

Evaluation and application of a new scintillator-based heat-resistant back-scattered electron detector during heat treatment in the scanning electron microscope

R. Podor¹  | J. Mendonça^{1,2} | J. Lautru¹ | H. P. Brau¹ | D. Nogues² | A. Candeias² | P. Horodysky³ | A. Kolouch³ | M. Barreau⁴ | X. Carrier⁴ | N. Ramenatte⁵ | S. Mathieu⁵ | M. Vilasi⁵

¹ ICSM, Univ Montpellier, CNRS, ENSCM, CEA, Bagnols sur Cèze, France

² NewTEC Scientific, Nîmes, France

³ CRYTUR, spol. s.r.o., Czech Republic

⁴ Laboratoire de Réactivité de Surface, CNRS, Sorbonne Université, Paris, France

⁵ CNRS, IJL, Université de Lorraine, Nancy, France

Correspondence

Renaud Podor, ICSM, Univ Montpellier, CEA, CNRS, ENSCM, 5257 Site de Marcoule, Bâtiment 426 BP 17171, F-30207 Bagnols sur Cèze Cedex, France.
Email: Renaud.podor@cea.fr

Funding information

Région Occitanie, Grant/Award Number: Readynov Furna SEM Project

Abstract

A new high-temperature detector dedicated to the collection of backscattered electrons is used in combination with heating stages up to 1050°C, in high-vacuum and low-vacuum modes in order to evaluate its possibilities through signal-to-noise ratio measurements and different applications. Four examples of material transformations occurring at high temperature are herein reported: grain growth during annealing of a rolled platinum foil, recrystallisation of a multiphased alloy, oxidation of a Ni-based alloy and complex phase transformations occurring during the annealing of an Al-Si coated boron steel. The detector could be potentially adapted to any type of SEM and it offers good opportunities to perform high-temperature experiments in various atmospheres.

KEYWORDS

backscattered electrons, high temperature, in situ, scanning electron microscopy, VP-SEM

1 | INTRODUCTION

High-temperature reactivity is for many materials a huge topic that includes all the aspects of their life-time cycle, from their manufacturing to their use in service conditions until their degradation. Thus, there is a real need for tools allowing the direct observation of transformations and reactivity at high temperature at the microscopic scale in order to determine and quantify the involved mechanisms. Today, Transmission Electron Microscopy (TEM) coupled with heating holders^{1–4} is a growing field of interest that offers new insights into materials reactivity up to the atomic scale.^{5–10} Even if this technique brings new insights in physic and chemistry of materials, it remains limited to the observation of very small samples – that are generally not totally representative of the bulk material – or to the reactivity of nanoparticles.

In many applications, including materials oxidation, recrystallisation, ageing, solid-state reactivity, sintering etc, the reaction can be rapidly limited by the long-distance diffusion of elements (ie in the order of 1 to hundreds of micrometres, depending on time, temperature and material considered). Reliable evidences of the mechanisms can only be achieved by observing bulk materials, and not only thin foils or nanoparticles. Thus, for many scientific questions, high-temperature experiments in the TEM need to be complemented by SEM analysis in order to observe and to describe these transformations. For these studies, High-Temperature (Variable Pressure) Scanning Electron Microscopy (HT-SEM or HT-VPSEM) is a promising tool that could allow the scale up for the observation of reacting or dynamic surfaces.¹¹

This technique has been used for decades and many different scientific questions have been addressed.^{12–18}

Using a (VP)SEM, most of the collected information comes from two electron signals, secondary electrons (SE) and backscattered electrons (BSE) being the main electron emissions used to produce images. SE is generally associated to a topographic contrast while the contrasts observed in BSE images are associated to compositional variations. To date, in most cases, the secondary electrons are collected when the specimen is heated at high temperature (up to 1450°C), using direct collection (in vacuum) or using a SE signal amplification through a gas. Indeed, SE collection by the Everhart-Thornley Detector (ETD) is only possible when the sample is maintained in high vacuum.¹⁹ When gases are introduced in the (VP)SEM to react with the material to be studied, only Gaseous Detection Devices (GDD) can be used.^{20,21}

Standard BSE detectors cannot be used to collect directly the BSE signal emitted by a heated sample, as the emission of visible light, which becomes predominant when $T > 300^\circ\text{C}$, saturates these detectors. Thus, they lose their effectiveness – and can be destroyed – when they are heated. Danilatos²² has reviewed and compared the possibilities offered by Yttrium Alumina Garnet scintillators detectors for the BSE collection in the VP-SEM.^{23,24} He has proposed that they can be used at high temperature.

Several strategies have been adopted to collect images containing compositional information during HT experiments in a SEM. As an example, Bozzolo et al have heated a thin metal plate very fast (up to 1180°C), to anneal it for very short times at high temperature and to cool down (to quench) the specimen to room temperature (RT) very fast in order to freeze the high-temperature microstructure.²⁵ Then, the sample is characterised by EBSD at RT. This process can be repeated several times to observe fast microstructural transformations.

EBSD can also be performed directly at high temperature in the SEM chamber.^{26,27} First of all, in their pioneer work, Seward et al (2002) have collected the SE and BSE signals emitted by metal plates.²⁸ They have observed orientation contrasts of grains up to 900°C using a KE industries solid-state backscattered electron (BSE) detector (K.E. Developments Ltd., Cambridge, UK) and they have opened the possibility to record Electron Back Scattered Patterns (EBSD) at high temperature. Since this work, in situ EBSD at high temperature has been developed and used. Different strategies and configurations were developed as a function of the material investigated and transformation rates. Recent developments of fast EBSD recording allow describing precisely the microstructural transformations occurring at the micrometre²⁹ and submicrometre³⁰ scales, when observing the moving interphase boundaries between ferrite and austenite crystals.

Parallel, Joachimi et al³¹ have designed and manufactured a novel (BSE) detector, as well as an Electron Beam Absorbed Current detector³² combined with a high-temperature stage. This BSE detector is a light blind alternative to the standard BSE detector provided by replacing the sensing elements from semiconductor diodes to conductive absorption pads, and thus switching from induced to absorbed electron detection (AED). However, the electronics design has not been optimised for low signals, which results in a slow minimum dwell time in the range of a few microseconds per pixel for image recording, as mentioned by the authors. With these detectors they have observed material transformations occurring at 400°C.

New opportunities using Transmission Kikuchi Diffraction (TKD) have been opened for the structural study of thin samples (approx. 100 nm) in the SEM chamber.³³ Recently, TKD was operated on a sample deposited on a microelectromechanical system (MEMS)-based heating stage in order to characterise microstructural transformation on thin films. Important information has been collected to understand the first steps of dewetting.³⁴ However, this technique does not offer the possibility to observe the transformations of bulk materials as it requires electron transparent samples such as thin films or thin foils. Further possibilities for low-energy nanodiffraction in the SEM, with a possible extension at high temperature, have also been reported.³⁵ These technical developments can bring new opportunities to observe precisely crystallographic transitions occurring at high temperature directly in the SEM chamber.

These technical solutions have brought new insights on the materials behaviour at high temperature. However, when available (on the Camscan X500 Crystal Probe-Obducat CamScan Ltd., Cambridgeshire, UK), backscattered electron collection was only used for orientation contrast imaging.²⁸ Thus, there is a real need for a special design that allows combining high-temperature scanning electron microscopy with true BSE collection. We herein propose to use an Yttrium Alumina Garnet (YAG) BSE detector, as already suggested by Danilatos,²² to collect the BSE emission generated during the electron beam/matter interaction at high temperature. This detector is energy selective, thus electron beam and heat-induced SE emissions (which energies are much lower than the energy of backscattered electrons) are not collected by this detector. In the present study, this YAG detector is evaluated in different working conditions (vacuum, gases) at high temperature. The main aim of this work is to determine the possibilities offered by this detector in terms of image quality (signal-to-noise ratio and resolution) as well as its limits in operational conditions (maximum temperature, gas pressure etc). To achieve this goal, four distinct experiments and a series of complementary measurements have been

performed to show the promising applications of the detector, at different temperatures and under different gas pressure and gas nature.

2 | MATERIALS AND METHODS

2.1 | Environmental scanning electron microscope (ESEM)

A Quanta 200 ESEM FEG (FEI CompanyTM, Eindhoven, the Netherlands) has been used to perform the high-temperature experiments. It has been equipped either with the HT 1400 heating stage (FEI CompanyTM) or the FurnaSEM 1000 heating stage (NewTEC ScientificTM).

2.2 | Description of the Karmen detector

The KarmenTM detector, which has been developed by the Crytur CompanyTM (Czech Republic) and specialised for the collection of BSE emission during sample heating at high temperature, is used in this study. A particular sealed feedthrough for the Karmen BSE high-temperature detector (Crytur company, Turnov, Czech Republic)³⁶ has been designed and installed on the ESEM. With this detector, the collection of backscattered electrons is achieved by using a single-crystalline scintillator. Its commercial name is CRY18.³⁷ The scintillation crystal is fully coated with a 100 nm Al thin layer in order to prevent the photomultiplier from external light signal e.g. generated by the heated sample. This also yields to the rejection of backscattered electrons with energies lower than roughly 5 keV, as a 100 nm thick Al layer absorbs most of 5 keV electron energy. The scintillation light is detected by a photomultiplier tube module. Then, it is converted to a video signal which is brought to the auxiliary input of the SEM. The surface that faces the heating stage is cooled by a heat-pipe cooling system. The limit temperature for the detector body itself is 60°C. This cooling system limits the degradation of the detector and the detector itself protects the objective lens from radiative heating. When the limit temperature is reached the detector is automatically retracted from the working position to protect the detector from overheating. There is no possibility for a bias to attract BSE as can be done for the SE signal. A schematic view of the Karmen detector is shown in Figure 1a.

The position of the BSE detector in the SEM chamber is controlled by the geometry of the detector itself. The active area of the scintillator is a ring of inner/outer diameter 3/13 mm. The solid angle of collected BSE signal is given by the z -position of the sample, which is typically 3–6 mm

below the BSE sensor. The thickness of the BSE sensor is 5 mm. Thus, minimum working distance is 7 mm. This means that there is a 1 mm fixed gap between the sensor and the pole-piece and that the minimum gap between the sample and the sensor is also 1 mm.

2.3 | High-temperature stages/combination of the Karmen detector with the heating stages

The HT 1400 heating stage has been used for some of the experiments performed in this study. It has been modified in order to control precisely the specimen temperature with a dedicated sample holder.³⁸ The heat protection of the objective lenses is ensured directly by the Karmen detector that is cooled down and limits the temperature increase in the VPSEM chamber. The secondary electron signal is collected using a Gaseous Detection Device (the Large Field Detector – LFD provided by FEI company) generally associated with the ‘Low Vac’ and ‘Environmental’ modes (Figure 1b). The maximum gas pressure in the chamber is 750 Pa.

The FurnaSEM 1000 heating stage³⁹ has been developed by the authors and the NewTEC Scientific company (Nîmes, France) to provide an alternative to the other commercial heating stages. This heating stage is mainly metallic and relatively small (included within a 40 mm diameter circle). It is particularly adapted to the study of flat specimens and the use in vacuum (but it can also be used in a gaseous atmosphere). The control of the specimen temperature is precise ($\pm 2^\circ\text{C}$ at $T = 232^\circ\text{C}$ – Sn melting point; $\pm 5^\circ\text{C}$ at $T = 661^\circ\text{C}$ – Al melting point) as a S-type thermocouple is included in the sample holder. When working in vacuum, it is combined with both Karmen detector and the classical Everhart – Thornley secondary electron detector (Figure 1c).

Depending on the type of furnace that is used, the working distance is ranging between 12 and 20 mm and the sample-to-detector distance is ranging between 2 and 10 mm.

2.4 | Image processing methods

Image processing was performed using the ImageJ software.⁴⁰ As the image series were always recorded in the same Region of Interest (ROI) of a sample, the images (of a same stack) were aligned using the SIFT plugin⁴¹ for comparison purposes. For some series (ie images recorded at different accelerating voltages), it was necessary to adjust the whole stack contrast using the Stack Contrast Adjustment plugin.⁴² When necessary,

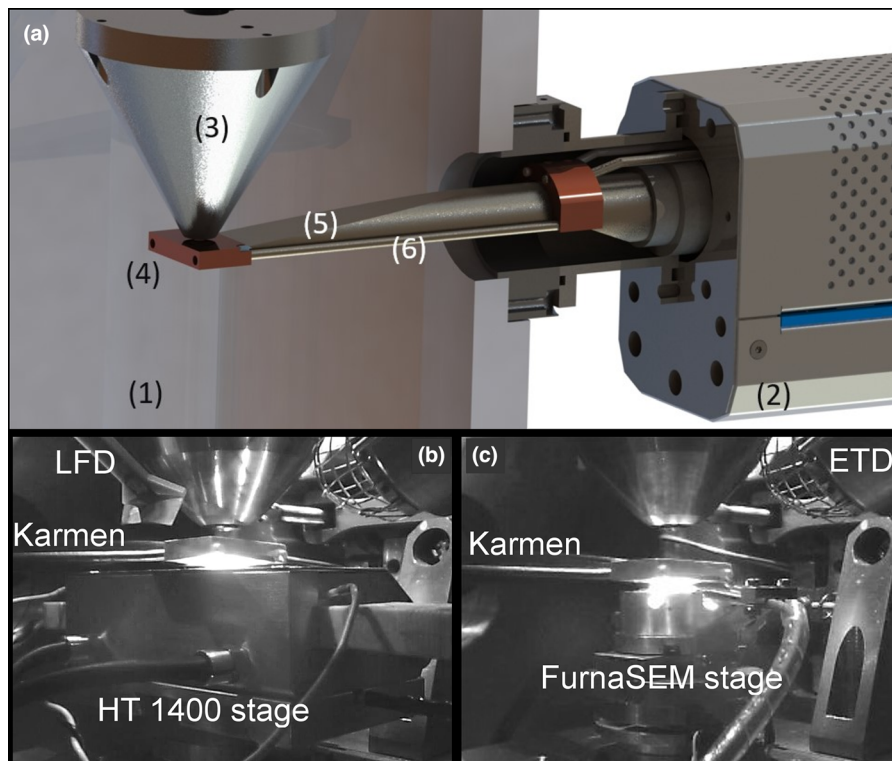


FIGURE 1 (a) Schematic view of the Karmen detector where (1) = SEM chamber, (2) = detector outer body, (3) = pole piece, (4) = scintillator + heat sink + external light shield, (5) = light-guide + external light shield, (6) = heat-pipe cooling system. Quanta 200 ESEM FEG (FEI company) chamber views of (b) a 'low vacuum' and 'environmental' working configuration with the HT1400 stage (FEI Company) + large field detector + Karmen detector and (c) a 'high vacuum' working configuration with the FurnaSEM 1000 stage (NewTEC Company) + Everhart-Thornley detector + Karmen detector, are reported

the images were processed using the SNR plugin⁴³ in order to systematically determine the signal-to-noise ratio (SNR) associated with each image in a series of images. In this case, the same reference image was always used. The quality of the image considered to be poor when the SNR value is lower than 15 dB. This value is arbitrary and depends on the quality of the reference image.

3 | RESULTS

3.1 | Operating parameter limits of the high-temperature BSE detector

During the present study, we have determined the main operating parameter limits of the high-temperature Karmen detector through different tests using the HT 1400 heating stage (Figure 1b) by measuring the SNR variations on different image series. The parameters that have been investigated were the accelerating voltage of the primary electron beam (expressed in kV), the frame rate (expressed in frame per second, as the frame size was 1024×884 pixels) and the air pressure in the VP-SEM chamber (expressed in Pa). These limits have been deter-

mined by modifying the experimental conditions using the BSE detector and by recording the images of the same region of interest on the specimen while varying the parameters. The working distance remains constant and equal to $19.0 (\pm 0.2)$ mm for these measurements. The main findings regarding the limits of the condition of use of the detector are reported below.

3.1.1 | Temperature

The maximum temperature which was reached in all conditions was 1050°C . One must note that in the explored temperature range, the resolution of the BSE image remains the same compared to that at room temperature. This will be illustrated later in the present study.

3.1.2 | Nature of the gases

Several experiments were performed in air, pure O_2 , vacuum and nitrogen. $\text{N}_2 + 4 \text{ vol.}\% \text{H}_2 + 2000 \text{ ppm H}_2\text{O}$ was also used for specific experiments.⁴⁴

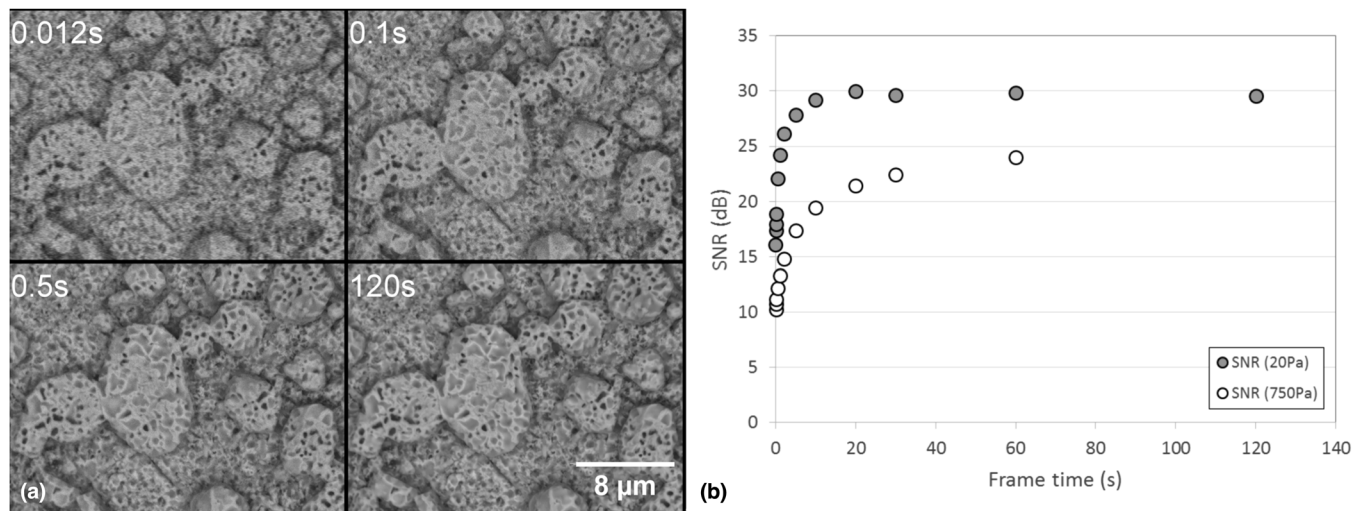


FIGURE 2 (a) Series of images recorded at $T = 500^{\circ}\text{C}$ on an Al-Si coated boron steel, in a 20 Pa air pressure, primary electron beam energy is 30 kV, with varying the frame time. (b) Values of signal-to-noise ratios (SNR) determined from the image series as a function of the frame time. The data are reported for 2 values of gas pressure in the VP-SEM chamber, 20 and 750 Pa

3.1.3 | Frame rate effect

One parameter that strongly influences the signal-to-noise ratio of the BSE images is the scan rate (here associated to the frame time). Two series of images were recorded at $T = 500^{\circ}\text{C}$ with frame times ranging between 12 milliseconds and 2 minutes, at 20 Pa (Figure 2a) and 750 Pa (see Supplementary Files S1a and S1b). The SNR results obtained are reported on Figure 2b. They clearly indicate that the higher the frame time, the better the signal-to-noise ratio. As an example, the SNR increases from 16.2 to 29.2 dB when the frame time is increased from 12 milliseconds to 10 seconds, with a total pressure of 20 Pa. The decrease of this parameter can be compensated by increasing both the electron beam current and the accelerating voltage of the electron beam. The balance between these parameters is limited by the decrease of the image resolution (with increasing accelerating voltage) as well as by the specimen sensitivity to the electron beam. The data obtained shows that the increase of the total gas pressure in the VPSEM chamber yields to a decrease of the SNR. As an example, when the frame time is equal to 30 seconds, the SNR is equal to 29.8 dB when $P = 20$ Pa whereas it is equal to 24.0 when $P = 750$ Pa (all the other parameters remain unchanged).

These data also indicate that images can be recorded at $T = 500^{\circ}\text{C}$ with very low frame times (corresponding to frame rates up to 80 images per second when the gas pressure in the chamber is equal to 20 Pa) while maintaining a SNR value higher than 15 dB. In these conditions, 100 nm large features remain observable – see the first image of Figure 2a recorded within 0.012 second – and very fast transformations of the sample can be observed.

3.1.4 | Gas pressure effect

BSE images can be recorded from high vacuum (10^{-3} Pa) up to a gas pressure of 750 Pa (which is the maximum value achievable in environmental conditions). An image series was recorded with different pressures, from 10 to 750 Pa of air, at $T = 500^{\circ}\text{C}$, with a constant frame time equal to 5 seconds and an accelerating voltage of 30 kV (Figure 3a). The SNR was systematically determined as a function of the gas pressure (Figure 3b). The movies corresponding to these experiments are reported in Supplementary Files S2a (BSE images) and S2b (SE images). The signal-to-noise ratio slowly decreases when the pressure increases in the VPSEM chamber. However, the SNR of the images remains higher than 15 dB even at high pressure. When the accelerating voltage was decreased to 12 kV, BSE images were recorded up to 300 Pa and a constant decrease of the SNR was measured with increasing air pressure (Supplementary File S2c). The SNR value remains higher than 15 dB up to 100–125 Pa (without modifying the frame time) and it decreased down to 11 dB when increasing the gas pressure in the chamber up to 300 Pa.

3.1.5 | Accelerating voltage effect

BSE images were recorded at high temperature using different accelerating voltage values ranging from 7 to 30 kV. A series of images recorded in 10 Pa air at $T = 900^{\circ}\text{C}$ is reported in Figure 4a (associated movie is reported in Supplementary File S3a). In this image series, the scan rates were adjusted to obtain high signal-to-noise ratios. One can see on the images that the depth of emission of

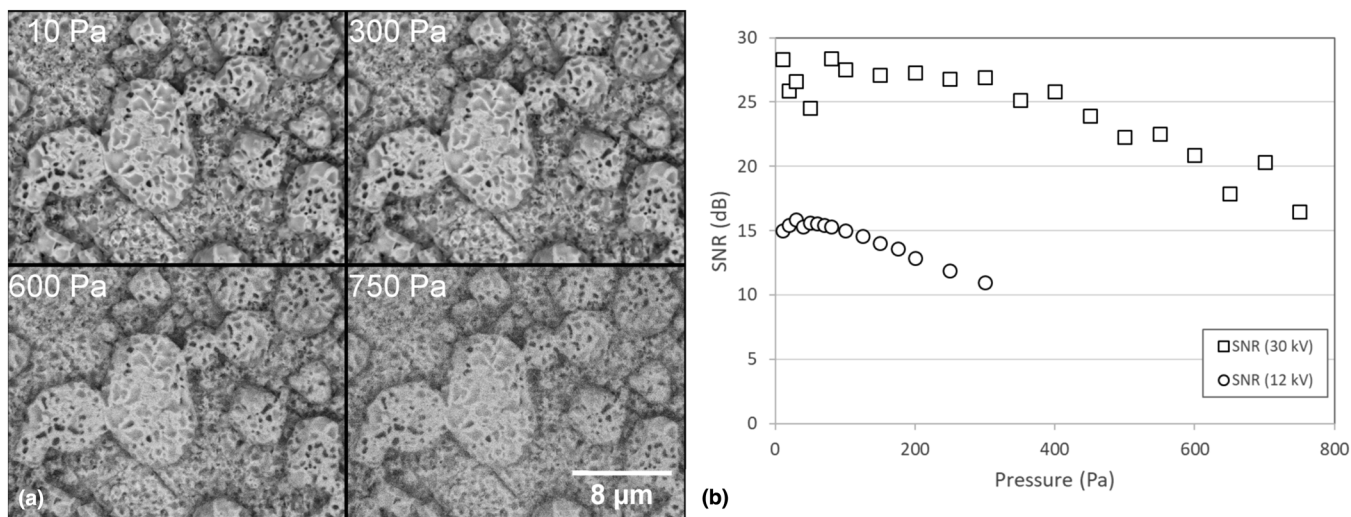


FIGURE 3 (a) Series of images recorded at $T = 500^\circ\text{C}$ on an Al-Si coated boron steel, in an air atmosphere, primary electron beam energy is 30 kV, with a 5-second frame time (the size an image is 1024×884 pixels). (b) Values of signal-to-noise ratios (SNR) determined from the image series as a function of gas pressure in the chamber and accelerating voltage

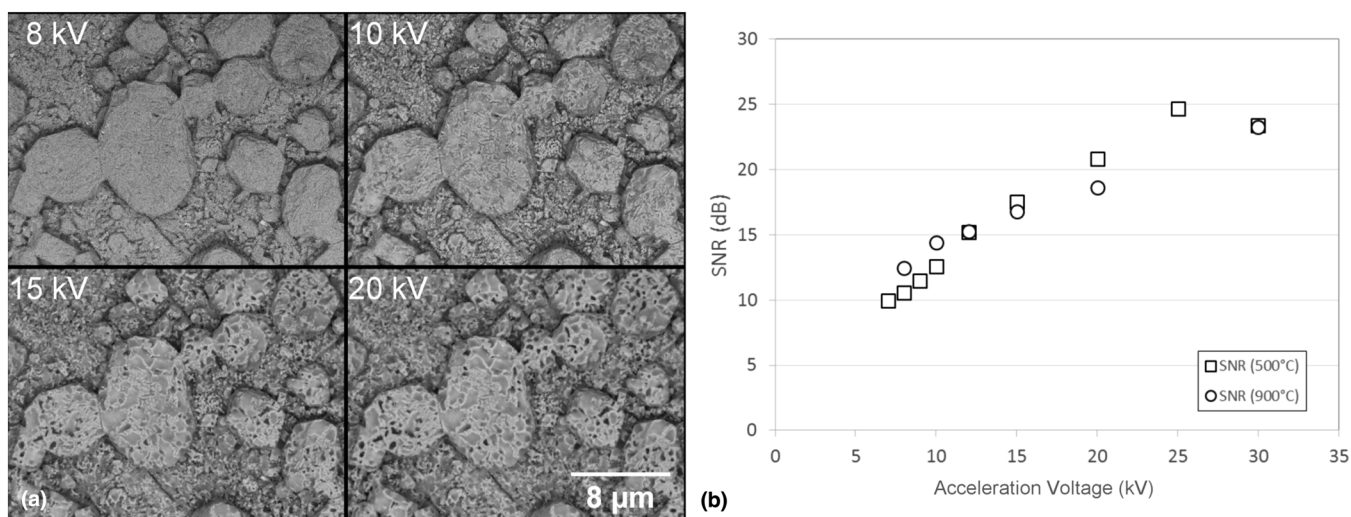


FIGURE 4 (a) Series of images recorded at $T = 900^\circ\text{C}$ on an Al-Si coated boron steel in 10 Pa air, with different values of the primary electron beam energy. The frame time is adjusted in order to optimize the SNR values. The corresponding frame times are 2 minutes, 1 minute, 30 seconds and 20 seconds for 8, 10, 15 and 20 kV, respectively. (b) SNR values determined from the image series recorded at $T = 500$ and 900°C . Frame time was fixed to 5 seconds, $P = 100$ Pa, for the series recorded at $T = 500^\circ\text{C}$

the BSE varies as usual with the energy of the primary electron beam. On the image recorded at 8 kV, the electrons are mainly emitted by the surface layers of the specimen, and the image obtained shows rather the specimen surface than a compositional contrast. At higher accelerating voltage (ie 20 kV), compositional contrasts probably corresponding to the presence of embedded phases or pores⁴⁵ are revealed as the primary electron beam penetrates deeper in the sample and the BSE escape depth is higher than at 8 kV. The BSE escape depths calculated by Monte Carlo simulations are 200 and 800 nm at 8 and 20 kV, respectively, in Si metal.⁴⁶ A second series of images

was recorded at 500°C , with a constant frame time equal to 5 seconds and in a gas pressure equal to 100 Pa. The finding is the same and in both cases, the SNR values increase linearly with the accelerating voltage (Figure 4b). Parallel, SE images were recorded. The associated movie is reported in Supplementary File S3b. Topographic contrasts are observable at low accelerating voltage (7 and 8 kV) on SE images while BSE images exhibit too low SNR values (lower than 11 dB) in the same conditions. At higher accelerating voltage, the SE and BSE images contain complementary information corresponding to topographic and compositional contrasts respectively.

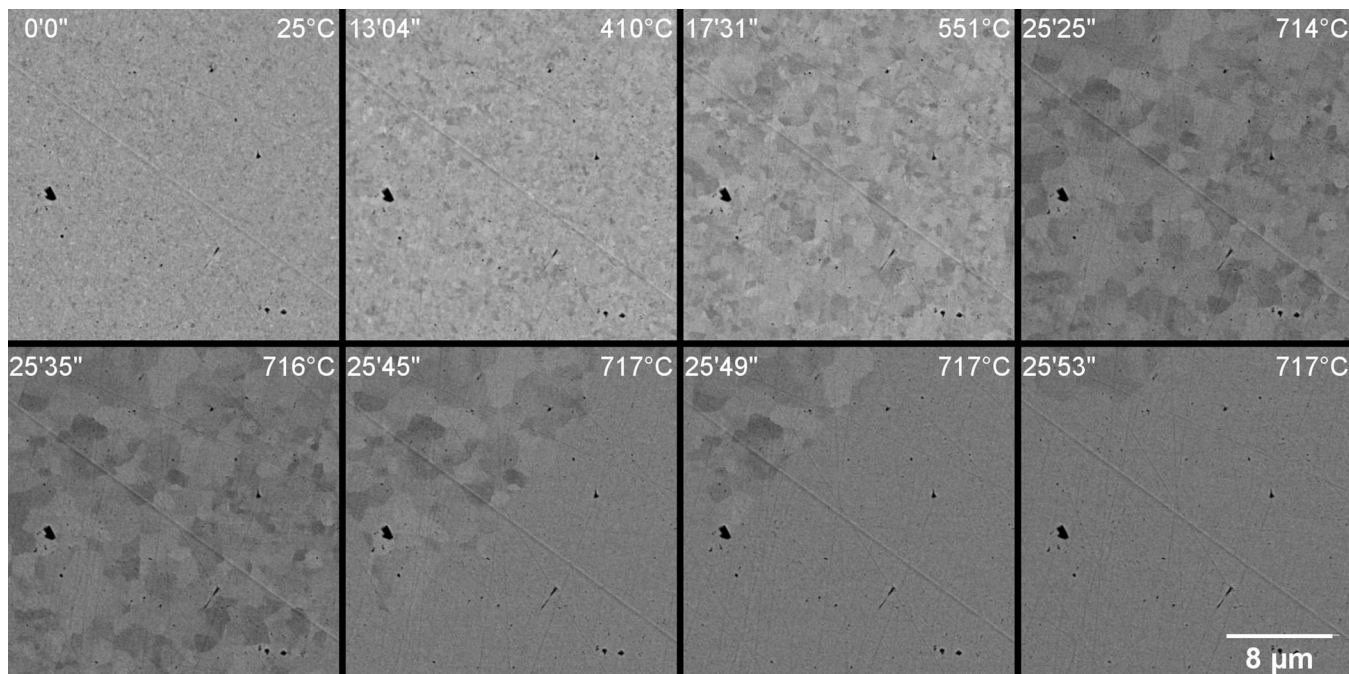


FIGURE 5 Annealing of a rolled Pt foil with a 27°C/min heating ramp. First line: normal grain growth and second line: abnormal grain growth

The operating possibilities of the high-temperature BSE detector were large enough to perform high-temperature experiments in a wide range of temperature and gas pressure, by potentially adapting the beam conditions (accelerating voltage, beam current) and frame time to the phenomenon to be observed. It is really interesting to note that a frame rate as low as 0.012 second can be achieved (Figure 2a). This offers the possibility to record high-speed images and to observe rapid transformations.

3.2 | Experiments performed using the high-temperature BSE detector

In order to screen the possibilities offered by the combination of the Karmen detector with the two heating stages and SE detectors, four different experiments have been achieved.

(1) Recrystallisation of a rolled Pt foil. The 500 μm thick as-rolled Pt foil (Goodfellow GmbH) initially contains small crystals (average diameter lower than 50 nm) with different crystallographic orientations. A $3 \times 3 \text{ mm}^2$ square sample is cut and polished to the 1 μm diamond. The polishing finishing is obtained with a 100 nm silica suspension. Sample annealing experiment is performed in vacuum with the FurnaSEM 1000 heating stage with a 25°C/min heating ramp. The beam conditions are 20 kV and a 14.4 mm working distance. BSE images are continuously recorded at different magnifications in order

to observe transformations that can occur at different scales.

The results obtained are reported as an image series (Figure 5). Complete series are also reported as movies in Supplementary Files S4a to S4d. These images illustrate the possibility to observe the recrystallisation processes that are generally not possible or very difficult to observe by high-temperature EBSD. For very fast phenomenon, it is necessary to cool down the sample to RT before recording EBSD patterns.²⁵ With this detector, it is possible to record very fast processes such as recrystallisation of Pt (up to a maximum of 80 images per second) but EBSD provides additional information (crystallographic orientation of grains) that cannot be derived from BSE orientation contrast images.

Using the BSE signal, it is possible to observe contrasts corresponding to different crystal orientations within the microstructure of the Pt foils and to describe precisely the recrystallisation processes. They are associated to grain growth during the 25°C/min annealing. The normal grain growth is observed first, in the 'low temperature' range, and it is characterised by a continuous growth of the grain size in the temperature range 450–700°C, that is below the $T/T_m = 0.5$ ratio generally accepted for an onset of the atomic diffusion in the metal lattice (T_m is the melting temperature of the metal). When this ratio is reached, fast abnormal grain growth is observed at higher temperature ($T = 717^\circ\text{C}$), with an acquisition period of 2 seconds per image (Figure 5). As expected, normal grain growth takes

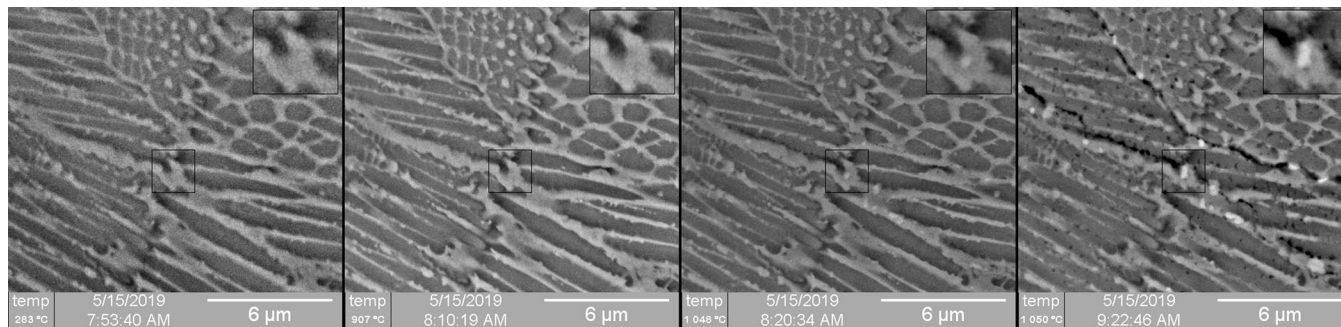


FIGURE 6 Series of images recorded at high temperature in high-vacuum conditions during the recrystallisation of multiphase high-temperature alloy using the Karmen BSE detector. The inset corresponds to a magnification of the $2 \times 2 \mu\text{m}^2$ central zone

place prior to abnormal grain growth.⁴⁷ This transition has recently been reported by Salanov et al (2019) but it has not been observed as precisely as reported herein.⁴⁸

This is to our knowledge the first time that images of so fast microstructural transformation (with a time step of 1–2 seconds between two images) are recorded in situ and that the fast grain growth can be observed directly. From these image series, and by developing appropriate image processing, several kinetic parameters that are characteristic of the processing observed on the images could be determined. These parameters could be relative with the determination of grain growth rates. The determination of the rate of grain boundary motions and the determination of the main kinetic and morphologic characteristics of the 2 steps processes will be reported and discussed in details in a future work.

(2) Recrystallisation of a multiphase high-temperature alloy. The sample is a nickel-based Inconel 625 ($\text{NiCr}_{22}\text{Mo}_9\text{Fe}_{4.3}\text{Nb}_{3.6}$ in wt %) manufactured using selective laser melting. The layer-by-layer fabrication stages yielded a microstructure characterised by very fine solidification structure. It results in small cells and elongated dendrites in parallel to the thermal gradient. The microstructure is highlighted by Mo and Nb segregations in the intercell and interdendritic spaces. The interdendritic distance is indicative of the very high cooling rate associated to the high laser scan rate employed (~ 90 cm/s). Its detailed microstructure is described elsewhere.⁴⁹ For the present investigation, the sample was thinned to 500 μm . Its surface was polished with 1 μm diamond paste and then with a 100 nm diameter silica suspension. Then, the sample is placed in the FurnSEM 1000 heating stage and annealed in vacuum with a 50 °C/min heating ramp up to 800 °C, then 20 °C/min up to 1050 °C. Note that this experiment was not possible to perform when using the HT 1400 heating stage. Indeed, in this configuration, gases are released by the heating stage (that contains porous ceramic components) with the temperature increase (until 1050 °C). Thus, the alloy reacts with the gases at high

temperature and this yields to the deterioration of its sub-surface microstructure by oxidation, when temperature is equal and higher than 950 °C.

The FurnSEM 1000 heating stage allows working in a very low vacuum (in the order of 10^{-3} Pa). A small piece of a Ti foil was also added close to the alloy sample to act as an oxygen getter. After the experiment, the Ti foil remained metallic and it only exhibits a light blue colour (indicating a very limited surface oxidation).

During the annealing, the alloy sample is not oxidised nor nitrided. Several images recorded at different temperatures and showing the microstructural modifications occurring during sample annealing are reported in Figure 6. Complete image series are reported in Supplementary Files S5a to S5d. The initial microstructure of the alloy remained stable up to 907 °C. When prolonging the annealing to 1050 °C, as evidenced by additional EBSD measurements, those selective laser melting materials contain a small amount of dislocations compared to mechanically deformed materials.⁵⁰ Therefore, their recrystallisation rate at 1050 °C is probably low and requires longer annealing or a higher annealing temperature to be complete. Unfortunately, the highest temperature that can be reached by this heating stage is too low. Indeed, this specific material has not stored enough energy for allowing the initiation of the recrystallisation process. However, the implementation of those in situ BSE observations prove to be perfectly suited to highlight the grain boundaries, and consequently their mobility, when recrystallisation processes have to be characterised at 1050 °C. This is notably the case of mechanically deformed Ni-based alloys which contain a dense dislocation network.

Moreover, those BSE observations showed the in situ thermal etching of the chromium-rich superalloy which happens in vacuum. The latter is due to a weak sublimation of chromium which is favoured at the grain and dendrite boundaries where the solid-state diffusion of chromium is high compared to the other elements that are present in the bulk. This process leads to a slight recess of the

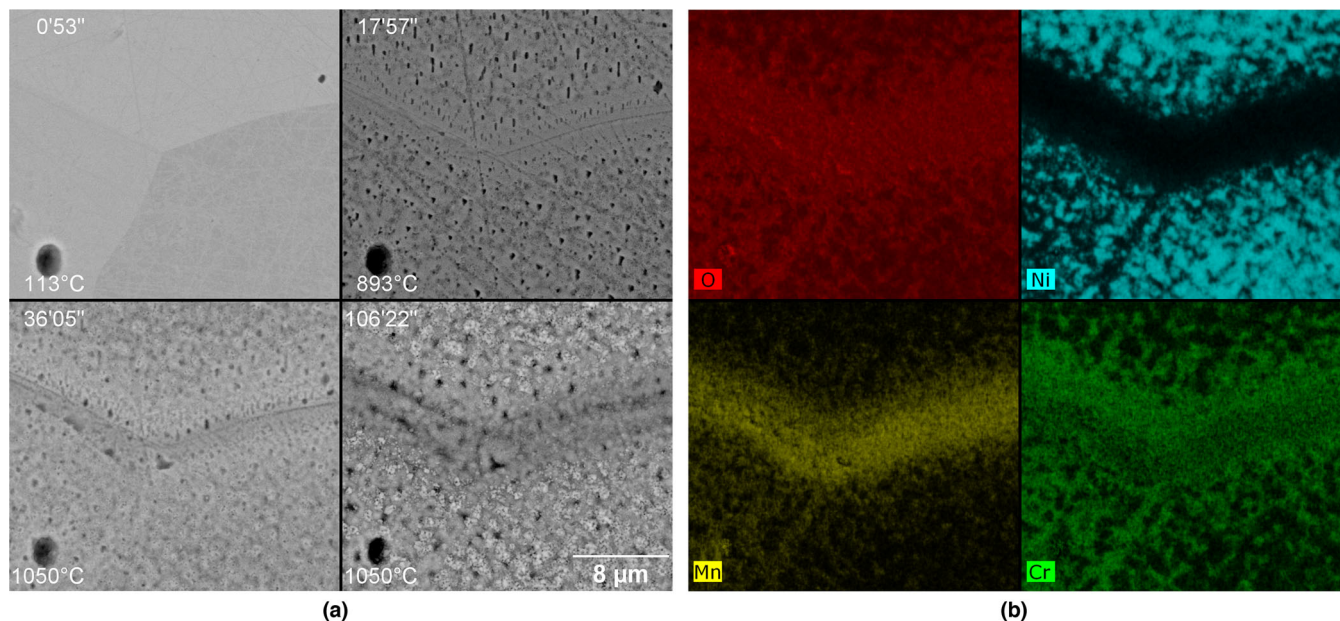


FIGURE 7 (a) High-magnification images of the oxidation of a Ni-25Cr-1.5Mn alloy in 50 Pa air up to 1050°C. (b) X-ray quantitative maps [Ni ($L\alpha$ line), Mn ($L\alpha$ line), Cr ($L\alpha$ line) and O ($K\alpha$ line)] recorded after sample cooling to room temperature on the region of interest observed at 1050°C, $t = 106'22''$, ($E_0 = 8$ kV)

intergranular and interdendritic zones which highlights the periphery of the grains and dendrites.

The direct observations of the microstructure of materials (case of Inconel 625 alloy) as well as the microstructural transformations (case of Pt foil) clearly illustrate the possibilities offered by the combination of FurnaSEM 1000 with the Karmen detector in the field of metallurgy. Precise and local studies can be performed to describe the effect of heat treatment on the evolution of alloy or metal microstructures.

(3) Oxidation of a Ni-25Cr-1.5Mn alloy in 50 Pa air up to 1050°C. A complete description of the oxidation process and formation of oxide layers is reported elsewhere.^{51,52} The oxidation test was performed using the FurnaSEM 1000 stage combined with the Karmen BSE detector. The sample was heated with a 50°C/min heating ramp up to 800°C, then with a 20°C/min heating ramp up to 1050°C, in 50 Pa of air (ie a relatively low oxygen pressure when compared to the previous study which was performed at 200 Pa pure oxygen). Then, the temperature is maintained constant for one hour. The images were recorded at 20 kV.

The sample surface was prepared by polishing with a 1 μm diamond paste then with a 100 nm silica suspension. Before the oxidation test, the alloy surface is homogeneous. After the sample insertion in the ESEM chamber, images were recorded at different magnifications on a triple grain junction (Figure 7a). The complete image series are reported in Supplementary Files S6a to S6e.

The recorded images allow the direct observation of the beginning of the oxidation process at low tempera-

ture and low O₂ pressure. The variations of the BSE contrasts observed during the sample oxidation show the complexity of the processes that arise at the very beginning of the material oxidation. The formation of pores is first observed at the surface of the grains during the heating stage, whereas the area neighbouring grain boundaries looks unaffected by this phenomenon. A complex oxide layer with several oxides forms at 1050°C as deduced of the different grey levels appearing on the BSE image. When combined with X-ray maps recorded after the experiment (after sample cooling to room temperature), it can be observed that the oxides contain different amounts of Cr, Ni and Mn (Figure 7b).

The details of the oxidation mechanism are reported by Perez.⁵³ The main features of the series of images reported herein are consistent with that mechanism. Indeed, Perez⁵² evaluated the microstructure of the oxide scale with accuracy by using HRTEM coupled to the ASTAR measurement (EBSD-TEM like). Their results show a complex stratification consisting, from the atmosphere/oxide interface to the oxide/substrate interface, of a thin layer of MnCr₂O₄, followed by a thick layer of Cr₂O₃ made up of columnar grains and finally of a thin layer of equiaxed Cr₂O₃. Moreover, the photoelectrochemistry measurements prove this oxide layer is characterised by a n-type semiconductivity due to the main diffusion of Cr and Mn interstitial cations leading to an external growth of the oxide scale.

According to the previous pictures (Figure 7a), the main information is that the superficial layer of the oxide grows

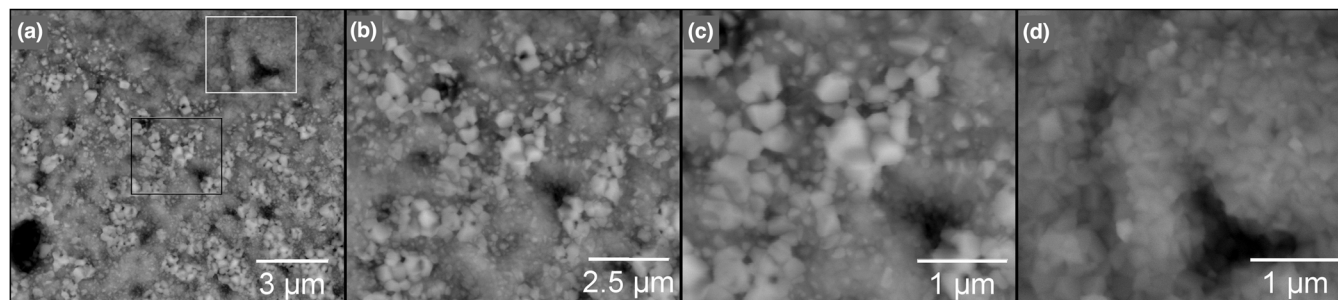


FIGURE 8 Images of the Ni-30Cr 1.5Mn alloy surface after oxidation at 1050°C in 50 Pa air in the ESEM chamber recorded at different magnifications and centered on the image reported on Figure 7. (a), (b) Details of the surface showing the different oxides. The black rectangle corresponds to zone C. The white rectangle corresponds to zone D

externally as depicted by the proposed mechanism. Therefore, it is kinetically controlled by the diffusion rate of the metallic constituents. In Figure 7a recorded at 893°C, the appearance of pores clearly indicates the arrival of metallic species by solid-state diffusion, too slow to counterbalance those oxidised. On the contrary, within the grain boundary, this kinetic limitation does not take place because the solid-state diffusion of metals is higher and therefore, the oxide seems denser and free of pores.

An image series recorded at 1050°C is reported on Figure 8 in order to highlight the resolution of the BSE images recorded at high magnification and at high temperature. Crystals as small as 100 nm long can be observed at 20 kV on Figure 8d.

(4) Temperature transformations of an Al-Si coated boron steel. The sample is a patented 22MnB5 steel covered by a 25 μm thick Al-Si coating⁵⁴ and it has been studied as received. Prior to the beginning of the experiment, X-ray maps of the elements Fe, Al, Si and O have been recorded in order to describe precisely the elements distribution in correlation with the BSE image (Supplementary File S7). The coating initial microstructure can be described as a matrix of aluminium with silicon rods, Al-Si alloys and Fe-Al-Si dendrites dispersed in it (Supplementary Files S8a and 8b). According to Maitra and Gupta,⁵⁵ those dendrites are composed of τ_5 ($\text{Fe}_2\text{Al}_{7.4}\text{Si}$) and τ_6 ($\text{Fe}_2\text{Al}_9\text{Si}_2$) phases, τ_6 crystallising in needle or rod shapes around τ_5 . The experiment has been performed in 20 Pa air atmosphere in order to collect both SE and BSE signals and to further correlate composition contrast with topographic contrast. The heating ramp was 15–20°C/min. During this experiment, the FurnaSEM 1000 heating stage was associated with the GDD that has been used for the SE collection and with the Karmen BSE detector for high temperature. The morphological modifications of the sample surface as well as the compositional variations were observed using both series of images, from room temperature up to 900°C, using a 12 kV accelerating voltage. The complete image series are reported as Supplementary Files S8a and S8b

where both BSE and SE images are gathered together for the same temperature. With these data, direct observation of the phase formation/transformations could be reported as a function of temperature. Selected BSE images that are representative of the different coating transformations are reported on Figure 9.

First, no significant modification is observed at the surface of the sample up to 550°C. Then, major transformations of the coating microstructure begin at $T = 550^\circ\text{C}$. Up to 600°C, the different transformations that occur do not modify significantly the topography of the sample surface, as observed on the SE images. These transformations have not been completely observed before when using secondary electrons⁴⁵ but their existence have been proposed by Podor et al (2020) while observing 3D modifications of the sample surface.⁵⁶ Among the new surface transformations observed using BSE in comparison with SE, it can be noticed that:

- At $T = 550^\circ\text{C}$, the beginning of large-scale modifications is observed at the surface of the coating on the BSE images. Large darker zones are formed starting from 550°C and they move as the temperature increases (see Figure 9a). These contrasts are associated to variations of the coating composition. They can be attributed to a partial oxidation of Al and formation of an Al_2O_3 protective layer.⁵⁷ This could be associated with the partial melting of the coating and/or dissolution of elements present in the alloy.
- Moreover, at $T = 550^\circ\text{C}$, after the dendrites dissolution (Fe-Al-Si ternary phases) already observed by Barreau et al,⁴⁵ the fast precipitation of acicular crystals that appears lighter than the surrounding liquid is observed. These crystals are then quickly dissolved into the liquid and they are not observed anymore when $T > 558^\circ\text{C}$ (Figure 9b). To our knowledge, it is the first time this phase transformation is observed. Regarding their specific shape, it is

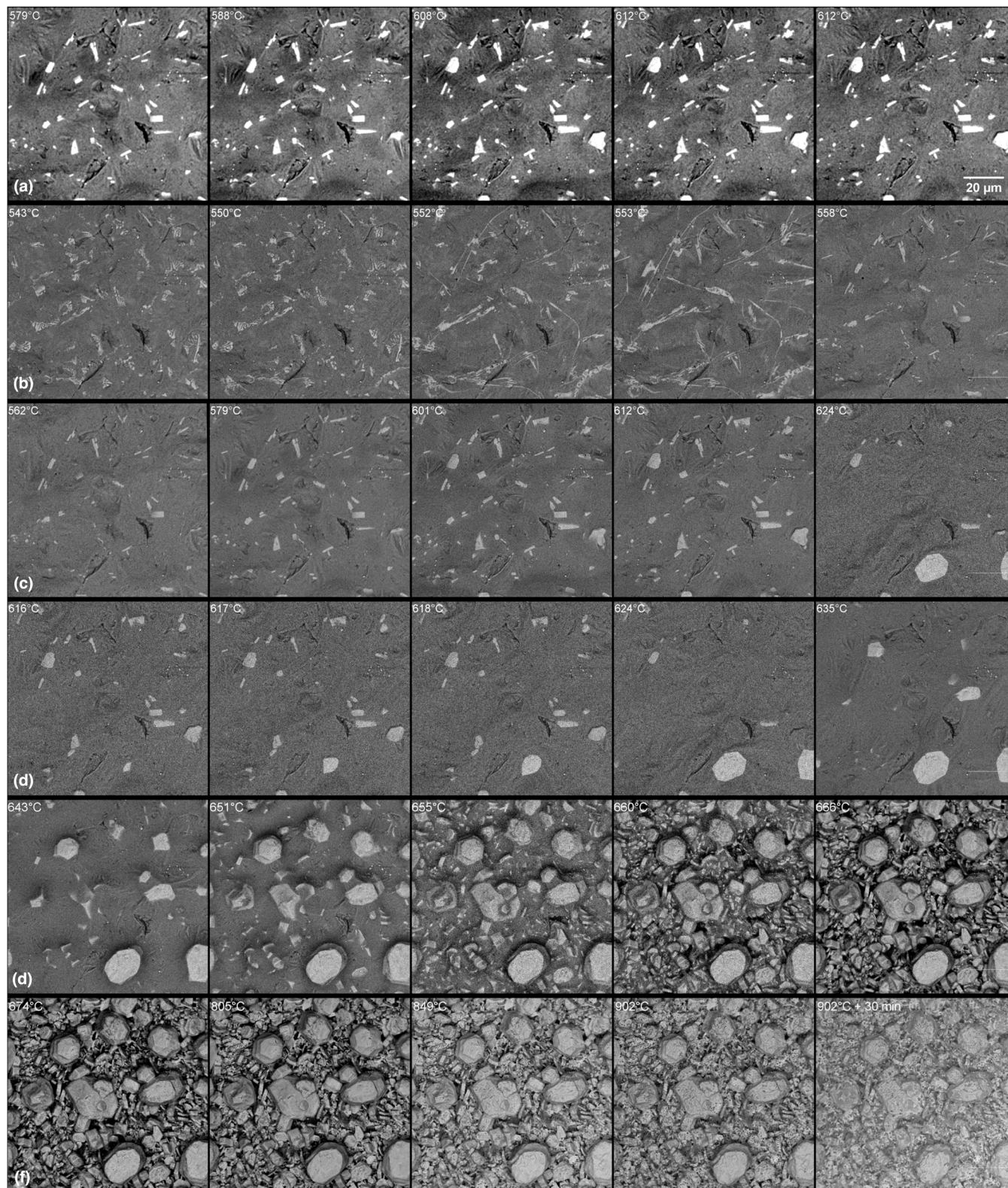


FIGURE 9 Heat treatment of an Al-Si coated steel from room temperature to 900°C with a 20°C/min heating ramp. Selected BSE images representative of the different observed transformations. (a) Variations of the BSE contrasts on the coating between 579 and 627°C. (b) First precipitation and dissolution of acicular crystals between 543 and 558°C. (c) Second precipitation and dissolution of square-shaped crystals between 562 and 624°C. (d) Third precipitation of hexagonal-shaped Fe-Al-Si τ_3 crystals between 616 and 635°C. (e) Fast phase formation due to the melting of the coating between 643°C and 666°C. (f) Slow solid-state transformations and oxidation of the surface phases between 674 and 902°C

hypothesised that these acicular crystals come from Si rods formation resulting from previous Fe-Al-Si phase dissolution.

- In the 560–616°C temperature range, the formation of a new Fe-Al-Si phase (probably mostly of τ_6 phase) that have a square shape is observed. These crystals are later dissolved in the liquid phase and they are not observed anymore when $T > 616^\circ\text{C}$ (Figure 9c).
- When temperature is ranging between 618 and 636°C, new crystals appear at the sample surface. These new hexagonal-shaped crystals will be the hills that will be observed at higher temperature (Figure 9d). As already described by Barreau et al, they result from the previous dissolution of τ_6 with Al leading to the formation of τ_5 (the only Fe-Al-Si phase crystallising in the hexagonal system).⁴⁵

These three steps are clearly observable on the BSE image series while they are more difficult to observe on the SE images as they are not directly correlated to clear topographic variations.

- When $635^\circ\text{C} > T > 673^\circ\text{C}$, the complete fusion of remaining aluminium is observed through the deformation of the coating surface (on both BSE and SE images). Fast transformations occur in this temperature domain. They quickly yield to the formation of hills at the same location of the hexagonal-shaped τ_5 phases formed at lower temperature. In the same time, the remaining liquid reacts with the substrate and new phases that have the form of platelets are formed. These transformations are very fast and they can be observed due to a very fast scanning rate achievable with the BSE detector. In this temperature range, the images were recorded with a frame time of 500 milliseconds. Despite a fast scanning rate, the quality of the BSE images remains good (with a signal-to-noise ratio higher than 15 dB) while the quality of the SE images is relatively poor (low signal-to-noise ratio yielding to very noisy images with few topographic contrast information). Only the BSE signal (collected with the Karmen detector) allows observing clearly these transformations (Figure 9e).
- When the temperature is above 675°C, slow chemical transformations occur through high-temperature reactivity and progressive iron diffusion from the steel to the surface (formation of Fe-enriched phases). They yield to limited but observable surface morphological variations. At $T = 900^\circ\text{C}$, the coating is annealed isothermally

for 30 minutes leading to the formation of porosity that have already been hypothesised to result from the formation of a crystallised $\alpha\text{-Al}_2\text{O}_3$ layer. They are observable on both SE and BSE images (Figure 9f).

4 | DISCUSSION

The comparison of both BSE and SE sets of images yields to the following general remarks. First, each type of image contains the expected information. BSE images recorded with the Karmen detector provide composition contrasts without any topographic information, as the SE signal is stopped by the 100 nm Al layer deposited at the detector surface. The Gaseous Detection Device used for SE collection provides images containing topographic information. There is no effect on the detectors of thermal ionic electron emission as well as light emission. Second, huge differences in the dynamic of the detectors are observed: using the GDD yields to the recording of very noisy images (due to the air pressure in the chamber which was limited to 20 Pa) when the frame rate is equal to – or below – 1 second while the quality of the BSE images remains good or acceptable (SNR value equal or below 15 dB). Trials to record BSE images with a frame rate of 80 images/second (with a 512 pixels large resolution) were successful and yielded to images with a SNR higher than 15 dB (see Figures 3a and 3b). This clearly paves the way to the direct observation of very fast transformations (high-speed high-temperature electron microscopy) that was not achievable up today with Gaseous Detection Devices. Third, BSE (and SE) images were recorded with the high voltage of 12 kV. However, it was possible to decrease the accelerating voltage down to 8 kV and to record images using the Karmen detector (Figure 5b).

The BSE images give a direct information of the phase formation/transformations occurring at the surface (approximately the first micrometre in depth) of the sample. Then, a complete description of these transformations can be proposed obviously regarding data obtained through other characterisation techniques (Thermal analysis methods – DTA/DTG, high-temperature X-ray diffraction etc). Moreover, the set of BSE images allows to observe and to describe phenomena that can occur in a very small temperature window. Indeed, during the heating of the Al-Si coating, one can observe the formation of acicular precipitates that further dissolve within an 8°C range between 550 and 558°C.

From all the data we have obtained during the present study, the main advantages of the Karmen BSE detector are listed hereafter:

- The detector can be attached with any type of SEM combined with a high-temperature stage and it allows working in the high-vacuum and low-vacuum modes.
- It allows (a) the collection of the back scattered electron signal emitted from a heated sample (b) while filtering the thermal electron emission and (c) it is not sensitive to heat and to light emission due to the black body emission.
- Furthermore, there is no need to protect the SEM chamber from thermal radiation (to a reasonable extend) as the Karmen detector directly plays the role of a heat shield. This remains true as long as the safety cooling fluid temperature is not reached. This approximately corresponds to a maximum sample temperature equal to 1000-1050°C.

By combining in situ BSE images with post mortem EDS analyses of the samples, it is possible to associate the BSE contrasts with the phase compositions and to propose clear chemical transformation pathways.

5 | CONCLUSIONS

A BSE detector developed and adapted for high-temperature experiments in a SEM has been tested in different experimental conditions under working conditions. We have demonstrated that it can be used in high vacuum, as well as in low-vacuum and environmental conditions (up to gas pressure remaining in the VP-SEM chamber equal to 750 Pa). The maximum temperature that has been reached with this detector is 1050°C. Neither supplementary heat shield nor thermal electron filter is required with this detector that is not sensitive to thermal electrons and to light emissions due to sample heating.

As a matter of fact, if associated with any heating stage, this detector could be potentially installed in any type of SEM. Thus, it will allow collecting backscattered electrons at high temperature in the presence of gases in the SEM chamber. This truly offers new opportunities to develop high-temperature experiments in gaseous atmospheres, even when using a conventional SEM which can work in a 'low vacuum' mode.

ACKNOWLEDGMENTS

This work was financially supported by the Région Occitanie (France) through the Readynov FurnaSEM project.

ORCID

R. Podor  <https://orcid.org/0000-0002-8103-1743>

REFERENCES

1. DENS Solutions. Wildfire – In situ TEM heating real-time imaging of thermal dynamics. Retrieved from <https://denssolutions.com/products/wildfire/>
2. ThermoFisher Scientific. NanoEx-i/v – A single-tilt TEM specimen heating and biasing holder for in situ S/TEM imaging and elemental analysis at elevated temperatures. Retrieved from <https://www.fei.com/accessories/nanoEx-i-v/>.
3. Protochips, Fusion Select – A user configurable in situ heating and electrical characterization system. Retrieved from <https://www.protochips.com/products/fusion/>.
4. Hummingbird Scientific. MEMS Heating + Biasing. Retrieved from <http://hummingbirdscientific.com/products/heating-biasing/>.
5. Denny, N. R., Li, F., Norris, D. J., & Stein, A. (2010). In situ high temperature TEM analysis of sintering in nanostructured tungsten and tungsten–molybdenum alloy photonic crystals. *Journal of Materials Chemistry*, 20, 1538–1545.
6. Asoro, M. A., Kovara, D., & Ferreira, P. J. (2014). Effect of surface carbon coating on sintering of silver nanoparticles: In situ TEM observations. *Chemical Communications*, 50, 4835–4838.
7. Baumgardner, W. J., Yu, Y., Hovden, R., Honrao, S., Henig, R. G., Abruña, H. D., ... Hanrath, T. (2014). Nanoparticle metamorphosis: An in situ high-temperature transmission electron microscopy study of the structural evolution of heterogeneous Au:Fe₂O₃ nanoparticles. *ACS Nano*, 8, 5315–5322.
8. Xue, C., Narushima, T., Ishida, Y., Tokunaga, T., & Yonezawa, T. (2014). Double-wall TiO₂ nanotube arrays: Enhanced photocatalytic activity and in situ TEM observations at high temperature. *ACS Applied Materials & Interfaces*, 6, 19924–19932.
9. Zhang, Y., Zhang, Z., Cheng, Y., Cheng, F., Wang, L., Liu, N., ... Gao, Y. (2020). In situ TEM observation of controlled growth of two-dimensional WS₂ with vertically aligned layers and high-temperature stability. *Nano Energy*, 67, 104221.
10. Chmielewski, A., Ricolleau, C., Alloyeau, D., Wang, G., & Nelayah, J. (2020). Nanoscale temperature measurement during temperature controlled in situ TEM using Al plasmon nanothermometry. *Ultramicroscopy*, 209, 112881.
11. Podor, R., Nkou Bouala, G. I., Ravau, J., Lautru, J., & Clavier, N. (2019). Working with the ESEM at high temperature. *Materials Characterization*, 151, 15–26.
12. Verma, S. K., Raynaud, G. M., & Rapp, R. A. (1981). Hot-stage scanning electron microscope for high-temperature in-situ oxidation studies. *Oxidation of Metals*, 15, 471–483.
13. Gregori, G., Kleebe, H. I., Siegelin, F., & Ziegler, G. (2002). In situ SEM imaging at temperatures as high as 1450°C. *Journal of Electron Microscopy*, 51, 347–352.
14. Podor, R., Clavier, N., Ravau, J., Claparède, L., Dacheux, N., & Bernache-Assollant, D. (2012). Dynamic aspects of cerium dioxide sintering: HT-ESEM study of grain growth and pore elimination. *Journal of the European Ceramic Society*, 32, 353–362.
15. Niania, M., Podor, R., Britton, T. B., Li, C., Cooper, S., Svetkov, N., ... Kilner, J. (2018). In-situ study of strontium segregation in LSCF in ambient atmospheres using HT-ESEM. *Journal of Materials Chemistry A*, 6, 14120–14135.

16. Song, B., Bertei, A., Wang, X., Cooper, S. J., Ruiz-Trejo, E., Chowdhury, R., ... Brandon, N. P. (2019). Unveiling the mechanisms of solid-state dewetting in Solid Oxide Cells with novel 2D electrodes. *Journal of Power Sources*, 420, 124–133.
17. Hieke, S. W., Willinger, M. G., Wang, Z. J., Richter, G., Chatain, D., Dehm, G., & Scheu, C. (2019). On pinning-depinning and microkink-flow in solid state dewetting: Insights by in-situ ESEM on Al thin films. *Acta Mater*, 165, 153–163.
18. Jacquet, P., Bouteille, B., Dezert, R., Lautru, J., Podor, R., Baron, A., ... Gozhyk, I. (2019). Periodic arrays of diamond-shaped silver nanoparticles: From scalable fabrication by template-assisted solid-state dewetting to tunable optical properties. *Advanced Functional Materials*, 29, 1901119.
19. Everhart, T. E., & Thornley, R. F. M. (1960). Wide-band detector for micro-microampere low energy electron currents. *Journal of Scientific Instruments*, 37, 246.
20. Danilatos, G. D. (1983). A gaseous detector device for an environmental SEM. *Micron and Microscopica Acta*, 14, 307–319.
21. Morgan, S. W. (2005). Gaseous secondary electron detection and cascade amplification in the environmental scanning electron microscope. PhD thesis, University of Technology, Sydney, Australia, 241 pp.
22. Danilatos, G. D. (2012). Backscattered electron detection in environmental SEM. *Journal of Microscopy*, 245, 171–185.
23. Autrata, R. (1989). Backscattered electron imaging using single crystal scintillator detectors. *Scanning Microscopy*, 3(3), 739–763.
24. Autrata, R., Herma, R., & Muller, M. (1992). An efficient single crystal BSE detector in SEM. *Scanning*, 14, 127–135.
25. Bozzolo, N., Jacomet, S., & Logé, R. E. (2012). Fast in-situ annealing stage coupled with EBSD: A suitable tool to observe quick recrystallization mechanisms. *Materials Characterization*, 70, 28–32.
26. Mirpuri, K., Wendrock, H., Menzel, S., Wetzig, K., & Szpunar, J. (2004). High temperature behavior of Cu films studied in-situ by Electron Backscatter Diffraction. *Microelectronic Engineering*, 76, 160–166.
27. Gourgues-Lorenzon, A. F. (2009). Application of electron backscatter diffraction to the study of phase transformations: Present and possible future. *Journal of Microscopy*, 233, 460–473.
28. Seward, G. G. E., Prior, D. J., Wheeler, J., Celotto, S., Halliday, D. J. M., Paden, R. S., & Tye, M. R. (2002). High-temperature electron backscatter diffraction and scanning electron microscopy imaging techniques: In-situ investigations of dynamic processes. *Scanning*, 24, 232–240.
29. Farahani, H., Zijlstra, G., Mecozzi, M. G., Ocelík, V., & De Hosson, J. Th.M. (2019). In situ high-temperature EBSD and 3D phase field studies of the austenite–ferrite transformation in a medium Mn steel. *Microscopy and Microanalysis*, 25, 639–655.
30. Zijlstra, G., van Daalen, M. S. B., Vainchtein, D. I., Ocelík, V., & De Hosson, J. Th.M. (2017). Interphase boundary motion elucidated through in-situ high temperature electron back-scatter diffraction. *Materials & Design*, 132, 138–147.
31. Joachimi, W., Hemmleb, M., Grauel, U., Wang, Z. J., Willinger, M. G., & Moldovan, G. (2018). High temperature BSE and EBAC electronics for ESEM. *Microscopy and Microanalysis*, 24(1), 694–695.
32. Moldovan, G., Grauel, U., & Joachimi, W. (2016). Development of low noise quantitative EBAC imaging in FEGSEM. European Microscopy Congress 2016: Proceedings, Lyon, France, pp. 414–415.
33. Keller, R. R., & Geiss, R. H. (2012). Transmission EBSD from 10 nm domains in a scanning electron microscope. *Journal of Microscopy*, 245, 245–251.
34. Fanta, A. B., Todeschini, M., Burrows, A., Jansen, H., Damsgaard, C. D., Alimadadi, H., & Wagner, J. B. (2018). Elevated temperature transmission Kikuchi diffraction in the SEM. *Materials Characterization*, 139, 452–462.
35. Schweizer, P., Denninger, P., Dolle, C., & Spiecker, E. (2020). Low energy nano diffraction (LEND) – A versatile diffraction technique in SEM. *Ultramicroscopy*, 213, 122956.
36. KARMEN™ – Retractable BSE detector for hot stage. Retrieved from <https://www.crytur.cz/products/karmen-retractable-bse-detector-for-hot-stage/>.
37. CRY-018, the mixed rare-earth silicate single crystal scintillation material. Retrieved from <https://www.crytur.cz/materials/cry-18/>
38. Podor, R., Pailhon, D., Ravaux, J., & Brau, H. P. (2014). Development of an integrated thermocouple for the accurate sample temperature measurement during high temperature environmental scanning electron microscopy (HT-ESEM) experiments. *Microscopy and Microanalysis*, 21(2), 307–312.
39. Podor, R., Pailhon, D., Ravaux, J., & Brau, H. P. (2014). Development of an integrated thermocouple for the accurate sample temperature measurement during high temperature environmental scanning electron microscopy (HT-ESEM) experiments. *Microscopy and Microanalysis*, 21(2), 307–312. <https://newtec.fr/fr/furnasem/>
40. Schneider, C. A., Rasband, W. S., & Eliceiri, K. W. (2012). NIH Image to ImageJ: 25 years of image analysis. *Nature Methods*, 9, 671–675.
41. Lowe, D. (2004). Distinctive image features from scale-invariant keypoints. *International Journal of Computer Vision*, 60, 91–110.
42. Capek, M., Janacek, J., & Kubinova, L. (2006). Methods for compensation of the light attenuation with depth of images captured by a confocal microscope. *Microscopy Research and Technique*, 69, 624–635.
43. Sage, D., & Unser, M. (2003). Teaching image-processing programming in Java. *IEEE Signal Processing Magazine*, 20, 43–52.
44. Trillaud, V., Podor, R., Gossé, S., Mesbah, A., Dacheux, N., & Clavier, N. (2020). In situ study of UO_{2+x} sintering first step by high-temperature environmental scanning electron microscopy. *Journal of the European Ceramic Society*, 40(15), 5891–5899.
45. Barreau, M., Méthivier, C., Sturel, T., Podor, R., Lautru, J., Humblot, V., ... Carrier, X. (2020). In situ study of the surface changes in morphology, composition and structure during heat treatment of an Al-Si coated boron steel. *Materials Characterization*, 163, 110266.
46. Zarraoa, L., González, M. U., & San Paulo, A. (2019). Imaging low-dimensional nanostructures by very low voltage scanning electron microscopy: Ultra-shallow topography and depth-tunable material contrast. *Scientific Reports*, 9, 16263.
47. Roy, R. K., Kar, S., & Das, S. (2009). Evolution of microstructure and mechanical properties during annealing of cold-rolled AA8011 alloy. *Journal of Alloys and Compounds*, 468, 122–129.
48. Salanov, A. N., Kochurova, N. M., Serkova, A. N., Kalinkin, A. V., Isupova, L. A., & Parmon, V. N. (2019). Oxidation and recrystallization of platinum group metals (Pt, Pd, Rh) in oxygen. Surface and subsurface reconstruction of polycrystalline platinum

- during annealing in the O₂ atmosphere over the temperature range of 600–1400 K. *Applied Surface Science*, 490, 188–203.
49. Ramenatte, N., Vernouillet, A., Vande Put, A., Mathieu, S., Monceau, D., & Vilasi, M. (2020). A comparison of the high-temperature oxidation behaviour of conventional wrought and laser beam melted Inconel 625. *Corrosion Science*, 164, 108347.
 50. Ramenatte, N. (2020). Fonctionnalisation de surface de l'inconel 625 élaboré par fabrication additive fusion lit de poudre. PhD Thesis, University of Lorraine, France.
 51. Perez, T., Latu-Romain, L., Podor, R., Lautru, J., Parsa, Y., Mathieu, S., ... Wouters, Y. (2018). In situ oxide growth characterization of Mn-containing Ni–25Cr (wt%) model alloys at 1050°C. *Oxidation of Metals*, 89, 781–795.
 52. Perez, T., Ghanbaja, J., Mathieu, S., Latu-Romain, L., Vilasi, M., & Wouters, Y. (2020). Microstructural characterization of the protective oxide scale forming on Ni–25Cr–xMn (x = 0.5, 1 and 1.5% wt) in a 200 Pa O₂ environment at 1050°C. *Scripta Materialia*, 178, 176–180.
 53. Perez, T. (2019). Oxydation à haute température d'alliages modèles Ni25Cr, Influence des éléments mineurs Al, Mn, Si sur les mécanismes de croissance des oxydes protecteur. PhD Thesis, University of Lorraine, France.
 54. Laurent, J. P., Hennechart, J. P., Spohner, D., & Devroc, J. (2001). Coated hot- and cold-rolled steel sheet comprising a very high resistance after thermal treatment. Patent n°US6296805B1.
 55. Maitra, T., & Gupta, S. P. (2002). Intermetallic compound formation in Fe–Al–Si ternary system: Part II. *Materials Characterization*, 49, 293–311.
 56. Podor, R., Le Goff, X. F., Lautru, J., Brau, H. P., Barreau, M., Carrier, X., ... Candeias, A. (2020). Direct observation of the surface topography at high temperature with SEM. *Microscopy and Microanalysis*, 26, 397–402.
 57. Pedraza, F., & Podor, R. (2016). Influence of annealing conditions on the formation of hollow Al₂O₃ microspheres studied by in situ ESEM. *Materials Characterization*, 113, 198–206.

SUPPORTING INFORMATION

Additional supporting information may be found online in the Supporting Information section at the end of the article.

How to cite this article: Podor R, Mendonça J, Lautru J, et al. Evaluation and application of a new scintillator-based heat-resistant back-scattered electron detector during heat treatment in the scanning electron microscope. *Journal of Microscopy*. 2020;1-15.
<https://doi.org/10.1111/jmi.12979>